

IMECE2018-87876

LARGE-EDDY SIMULATIONS OF LOW PRESSURE TURBINE ENDWALL FLOW AND HEAT TRANSFER

Stephen Lynch

Mechanical & Nuclear Engineering
The Pennsylvania State University
University Park, PA, USA

ABSTRACT

Turbine airfoils are subject to strong secondary flows that produce total pressure loss and high surface heat transfer in the airfoil passage. The secondary flows arise from the high overall flow turning acting on the incoming boundary layer, as well as the generation of a horseshoe vortex at the leading edge of the airfoil. Prediction of the effects of secondary flows on endwall heat transfer using steady Reynolds-averaged Navier-Stokes (RANS) approaches has so far been somewhat unsatisfactory, but it is unclear whether this is due to unsteadiness of the secondary flow, modeling assumptions (such as the Boussinesq approximation and Reynolds analogy), strongly non-equilibrium boundary layer behavior in the highly skewed endwall flow, or some combination of all. To address some of these questions, and to determine the efficacy of higher-fidelity computational approaches to predict endwall heat transfer, a low pressure turbine cascade was modeled using a wall-modeled Large Eddy Simulation (LES) approach. The result was compared to a steady Reynolds-stress modeling (RSM) approach, and to experimental data. Results indicate that the effect of the unsteadiness of the pressure side leg of the horseshoe vortex results in a broad distribution of heat transfer in the front of the passage, and high heat transfer on the aft suction side corner, which is not predicted by steady RANS. However, the time-mean heat transfer is still not well predicted due to slight differences in the secondary flow pattern. Turbulence quantities in the blade passage agree fairly well to prior measurements and highlight the effect of the strong passage curvature on the endwall boundary layer, but the LES approach here overpredicts turbulence in the secondary flow at the cascade outlet due to a thick airfoil suction side boundary layer. Overall, more work remains to identify the specific model deficiencies in RSM or wall-modeled LES approaches.

INTRODUCTION

In a gas turbine engine, the upper and lower walls (casing and hub, respectively) that contain the flow also result in the generation of boundary layers. These boundary layers reduce the overall performance of the turbomachine and generate complex flow patterns in the airfoil passage, known as secondary flow.

Secondary flow consists of several interconnected flow features. When the endwall boundary layer encounters the blockage of a turbine airfoil, it will separate and form coherent vorticity known as the horseshoe vortex, with two legs that wrap around the airfoil. Within the passage, strong flow turning causes development of a passage vortex that travels from the pressure to suction side. This often merges with the pressure side leg of the horseshoe vortex which has the same sense of rotation. The strong streamwise vorticity sweeps up endwall boundary layer fluid in the passage, as well as airfoil suction side boundary layer fluid as it encounters and climbs the airfoil suction side. The entrainment of endwall and suction side boundary layer fluid results in significant mixing and entropy generation, which leads to reduced aerodynamic performance. Furthermore, the sweeping action of the passage vortex can locally enhance heat transfer and remove cooling flow from the endwall.

Prediction of this behavior remains challenging due to the complex nature of the vortex evolution, possible unsteadiness, and transitional behavior of the endwall boundary layer inside the passage. As such, turbulent-scale-modeling computational approaches such as Reynolds-averaged Navier-Stokes (RANS) suffer from deficiencies. Higher-fidelity approaches such as large eddy simulation (LES) can be more accurate, but much more costly. It is of interest to evaluate what kinds of improvement in accuracy might be achievable with high-fidelity methods.

NOMENCLATURE

C_{ax} axial chord of blade

C_f	friction coefficient, $C_f = \frac{\tau_w}{1/2\rho U_{in}^2}$
C_p	specific heat, or static pressure coefficient
h	heat transfer coefficient, $h = \frac{q''}{T_w - T_{in}}$
k	turbulent kinetic energy, $k = \frac{1}{2} \left(\overline{u'u'} + \overline{v'v'} + \overline{w'w'} \right)$
P	blade pitch, or static pressure
Pr_{SGS}	subgrid-scale turbulent Prandtl number
Pr_t	turbulent Prandtl number
q''	wall heat flux
RSM	Reynolds stress model
Re_θ	momentum thickness Reynolds number, $Re_\theta = \frac{U_{in}\theta}{\nu}$
RSM	Reynolds Stress Model
s	surface distance
S	blade span, or strain rate tensor
St	Stanton number, $St = \frac{h}{\rho c_p U_{in}}$
T	temperature
Tu	freestream turbulence level, $Tu = \overline{u'}/U_{in}$
x, y, z	cascade coordinates
u, v, w	mean velocity components in cascade coordinates
u_τ	friction velocity, $u_\tau = \sqrt{\tau_w/\rho}$
U_{in}	magnitude of inlet streamwise velocity
$ V $	magnitude of mean velocity
V_s, V_n, V_z	velocity components in midspan coordinates

Greek

α	thermal diffusivity, or turbulence model constant
β	mean flow angle, or turbulence model constant
δ_{99}	boundary layer thickness (99%)
δ_{ij}	Kronecker delta
θ	momentum thickness
μ_{SGS}	subgrid-scale turbulent viscosity
μ_t	turbulent viscosity
ν	kinematic viscosity
ρ	density
σ	turbulence model constant
τ_w	wall shear stress
ω	specific dissipation

Superscript/Subscript

+	inner coordinates
'	fluctuating component
-	time-average
w	wall quantity

LITERATURE REVIEW

The secondary flow in a turbine cascade has been well studied in a time average sense, both experimentally and computationally. Early works [1-5] identified major flow structures generated in the airfoil passage, including the horseshoe vortex upstream of the leading edge, the passage vortex, suction side and pressure side corner vortices, and the trailing shed vorticity. These are strongly linked to aerodynamic

losses [1, 5-7] and high endwall heat transfer [8-13]. It is desirable to minimize secondary flows, and many active (blowing) [14, 15] and passive mechanisms (fillets [16, 17], endwall contouring [12, 18-23], fences [24, 25]) have been investigated, with varying degrees of success.

The state of the endwall boundary layer in a turbine passage is rather complex and likely transitional, which complicates predictions of secondary flow but even more so the surface skin friction and heat transfer. Hot-wire measurements by Langston [1] indicated a thin laminar-like boundary layer on the endwall downstream of the inlet boundary layer separation. Hot-film signals obtained downstream of the horseshoe vortex separation by Harrison [26] and Vera [27] exhibited much lower RMS values as compared to the upstream turbulent boundary layer, suggesting laminar-like flow. Holley and Langston [28] also reported low friction coefficients in this region, consistent with laminar flow. Laser Doppler velocimeter measurements by Lynch [29] suggested laminar boundary layer profiles near the exit of the cascade, although the measurements were limited in near-wall resolution.

Predictions of secondary flow effects using RANS approaches have had mixed results depending on the parameter of interest. Many researchers [5, 22, 30, 31] find that RANS can adequately predict the development of the mean secondary flowfield but struggles to predict aerodynamic losses in the secondary flow region, due to misprediction of mixing. Likely this is due to the complexity of the endwall flow; Lien and Leschziner [32] modified a k -epsilon turbulence model to enable transitional behavior tuned to a flat plate but still overpredicted aerodynamic losses due to early transition prediction in the blade passage.

More recently, computational studies have moved toward predictions of turbine flow using higher-fidelity approaches. Rao et al. [33] simulated the transition process of the suction side boundary layer in a low pressure turbine in the presence of freestream turbulence and wakes using LES. A series of studies by Gross et al. [34-36] used implicit LES to model endwall secondary flow in a high lift low pressure turbine. A particularly interesting finding of [37] is the intermittent breakdown of the passage vortex as triggered by the horseshoe vortex at the blade leading edge. Cui et al. [38] simulated low pressure turbine secondary flow using LES with three different inlet conditions (laminar boundary layer, turbulent boundary layer, and wake from upstream row) and found that the exit total pressure loss increased substantially for the turbulent and wake inlet conditions due to increased mixing. Reviews by Tucker [39, 40] considered the state of the art in RANS as well as the future outlook of scale-resolving simulations.

The intent of this study is to investigate the improvement in predictions of endwall heat transfer and turbulent flow in a turbine cascade using a scale resolving simulation, as well as a Reynolds-stress modeling simulation of lower computational cost. Few studies to date have considered the ability of high-fidelity CFD simulations to capture endwall heat transfer in a turbine passage. One possible reason is the dearth of complete

data sets that include inlet boundary conditions, surface measurements, and mean and turbulent flowfield quantities.

COMPUTATIONAL METHODS

Two turbulence modeling approaches were examined in this work: a steady Reynolds-stress model (RSM) previously reported by Lynch [29], as well as a time-resolved wall-modeled large eddy simulation (LES) approach. Both are compared to the experimental results reported in [12, 29, 41].

The computational domain (see Figure 1) for both models were nearly the same, with the exception of the span dimension and the amount of grid upstream of the blade passage. For the RSM model, the domain inlet extended $3.5C_{ax}$ upstream to capture some velocity boundary layer development prior to the start of the thermal boundary layer at $2.8C_{ax}$ upstream, as was described in the experiment of Lynch et al. [12]. The airfoil span was exactly half of the experimental airfoil domain height ($S=0.275$ m) so that a symmetry condition could be used. For the LES model, the upstream length was reduced to $1.9C_{ax}$, and the span height was reduced to 0.2 m to minimize excessive cell count. These changes were not expected to impact the midspan static pressure distribution, since the span/chord ratio of the airfoil is very large. However, as will be shown, the reduced boundary layer development length does have an impact on the incoming conditions to the cascade. For both models, a symmetry plane was used at the airfoil midspan, and a constant heat flux of 1000 W/m^2 was applied to the bottom wall (endwall). The sidewalls of the domain were periodic to simulate an infinite cascade, and all other walls (including the airfoil) were adiabatic no-slip walls, as per the experiment of Lynch et al. [12]. The cascade coordinate system origin is at the airfoil leading edge-endwall junction, with x as the axial direction, y as the pitchwise direction, and z as the spanwise (normal to endwall) direction.

The RSM model setup and details were also described by Lynch [29], so only a brief summary is given here. Because the experiment was operated in a low-speed wind tunnel with exit Mach ~ 0.04 , the air is assumed to be incompressible but is modeled as an ideal gas to allow density changes with temperature. The steady incompressible Navier-Stokes equations in Reynolds-averaged form (Cartesian tensor notation, $1=x$, $2=y$, $3=z$) are:

$$\frac{\partial U_i}{\partial x_i} = 0 \quad \text{Eq. (1)}$$

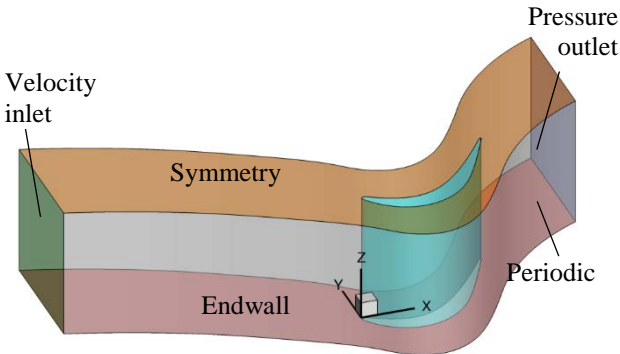


Figure 1. Computational domain.

$$U_j \frac{\partial U_i}{\partial x_j} = -\frac{1}{\rho} \frac{\partial p}{\partial x_i} + \frac{\partial}{\partial x_j} \left[\nu \left(\frac{\partial U_i}{\partial x_j} + \frac{\partial U_j}{\partial x_i} \right) - \overline{u'_i u'_j} \right] \quad \text{Eq. (2)}$$

$$U_j \frac{\partial T}{\partial x_j} = \frac{\partial}{\partial x_j} \left[\alpha \frac{\partial T}{\partial x_j} - \overline{u'_j T'} \right] \quad \text{Eq. (3)}$$

where Eq. (1) is continuity, Eq. (2) is the three momentum components, and Eq. (3) is the energy equation (viscous dissipation is not modeled due to the low Mach number). The Reynolds stress tensor terms in Eq. (4) are also modeled directly using the stress-omega formulation as implemented in Ansys Fluent [42]:

$$U_k \frac{\partial (\overline{u'_i u'_j})}{\partial x_k} = \frac{\partial}{\partial x_k} \left[\left(\nu + \frac{\mu_t}{\rho \sigma_k} \right) \frac{\partial (\overline{u'_i u'_j})}{\partial x_k} \right] - \left[(\overline{u'_i u'_k}) \frac{\partial U_j}{\partial x_k} + (\overline{u'_j u'_k}) \frac{\partial U_i}{\partial x_k} \right] + \left[p' \left(\frac{\partial u'_i}{\partial x_j} + \frac{\partial u'_j}{\partial x_i} \right) \right] - \left[\frac{2}{3} \delta_{ij} \beta_{RSM}^* k \omega \right] \quad \text{Eq. (4)}$$

The pressure-strain term (third bracketed term on the right) is modeled using a linear combination of the contribution of slow and rapid pressure-strain effects, while wall reflection effects are not necessary to model due to the use of the specific dissipation and its properties close to a wall (see [42] for details). The last bracketed term on the right side of Eq. (4) is the dissipation term based on the turbulent frequency (ω). Note that buoyancy production and rotation production terms are neglected here. The turbulent viscosity is:

$$\mu_t = \alpha^* \frac{\rho k}{\omega} \quad \text{Eq. (5)}$$

where α^* is a damping coefficient for the turbulent viscosity enabling correct low-Reynolds number behavior very near the wall. Turbulent heat flux is determined by the Reynolds analogy:

$$-\overline{u'_j T'} = \frac{\mu_t}{\rho Pr_t} \frac{\partial T}{\partial x_j} \quad \text{Eq. (6)}$$

where Pr_t is the default value of 0.85. Finally, the turbulence frequency ω needed for the Reynolds stress and turbulent viscosity is obtained from a transport equation:

$$U_j \frac{\partial \omega}{\partial x_j} = \frac{\partial}{\partial x_j} \left[\left(\nu + \frac{\mu_t}{\rho \sigma_\omega} \right) \frac{\partial \omega}{\partial x_j} \right] + \left[\frac{\alpha}{\mu_t} (2\mu_t S_{ij} S_{ij}) \right] - [\beta_i \omega^2] + \left[2(1 - F_1) \frac{1}{\omega \sigma_{\omega,2}} \frac{\partial k}{\partial x_j} \frac{\partial \omega}{\partial x_j} \right] \quad \text{Eq. (7)}$$

All model constants and blending functions in the above equations are the default values in Fluent.

ANSYS Fluent, version 18 was used to solve the above equations using a steady RANS approach. A segregated pressure-based formulation, with the SIMPLE pressure-velocity coupling algorithm, was employed. Spatial gradients were cell-based using the least-squares option, and all solution quantities were discretized using second-order upwinding. Convergence of the simulations was determined by three metrics: normalized residuals for the conservation equations had to reach values lower than 10^{-4} (10^{-6} for energy); area-averaged Nusselt number on the endwall had to change less than 0.1% over 500 iterations; and mass-averaged exit total pressure downstream of the blade had to change less than 0.1% over 500 iterations.

As described in [29], a grid independence study was performed for the RSM model, and both the average endwall Nu and exit total pressure varied by less than 1% for mesh cell counts of 0.62, 1.2, and 3.1 million cells. The medium grid with 1.2 million cells was used in this study. Per the requirements of

the RSM stress-omega model, Δz^+ values for the spacing of the first grid point from a wall surface was kept below 1 and boundary layer mesh inflation rate was kept to 1.2 or less.

Boundary conditions for the velocity inlet at $3.5C_{ax}$ upstream of the blade were determined by ensuring that the computational model prediction matched an experimentally measured velocity profile at $2.33C_{ax}$ upstream of the blade. Further agreement with a measured profile at $1.0 C_{ax}$ will be shown later.

For the LES model, the implementation was the algebraic wall-modeled LES (WMLES) approach, where the lower part of the logarithmic region of the boundary layer uses a RANS model and the outer part of the boundary layer is modeled using LES. This reduces some of the strict requirements for streamwise and cross-stream grid resolution near the wall, although those were mostly maintained at levels appropriate for wall-resolved LES in this study. The mathematical formulation for the unsteady incompressible momentum equation is:

$$\frac{\partial u_i}{\partial t} + U_j \frac{\partial u_i}{\partial x_j} = -\frac{1}{\rho} \frac{\partial p}{\partial x_i} + \frac{\partial}{\partial x_j} \left[\nu \left(\frac{\partial u_i}{\partial x_j} + \frac{\partial u_j}{\partial x_i} \right) \right] - \frac{1}{\rho} \frac{\partial \tau_{ij}}{\partial x_j} \quad \text{Eq. (8)}$$

where τ_{ij} is the subgrid-scale stress due to the non-resolved turbulent scales, which must be modeled. This term is computed by using the Boussinesq hypothesis to relate the stress to the strain rate from the resolved scales (S_{ij}) by a subgrid-scale viscosity:

$$\tau_{ij} - \frac{1}{3} \tau_{kk} \delta_{ij} = -2\mu_{SGS} S_{ij} \quad \text{Eq. (9)}$$

A similar type of term arises in the energy equation, which is the subgrid-scale turbulent heat flux. The subgrid-scale turbulent heat flux is approximated in Fluent using the gradient hypothesis:

$$-\overline{u_j' T'} = \frac{\mu_{SGS}}{\rho Pr_{SGS}} \frac{\partial T}{\partial x_j} \quad \text{Eq. (10)}$$

where μ_{SGS} is the subgrid-scale turbulent viscosity, and Pr_{SGS} is the subgrid Prandtl number at a default value of 0.85. Finally, the subgrid-scale turbulent viscosity is calculated in the LES region, as well as in the RANS zone close to the wall, using a modified formulation of Shur, et al. [43]:

$$\frac{\mu_t}{\rho} = \min \left[(\kappa d_w)^2, (C_{smag} d_w)^2 \right] * |S - \Omega| * \left[1 - \exp\left[-(y^+/25)^3\right] \right] \quad \text{Eq. (11)}$$

where d_w is the wall distance, and $|S - \Omega|$ is the absolute value of the difference between the strain rate magnitude and the vorticity magnitude. This particular formulation is known as the stress-omega variant. All constants in the models were left at the default values in Fluent.

To comply with grid resolution requirements, the LES grid was significantly refined relative to the RSM model. The spacing of the first grid point from the wall (Δz^+) was kept less than 1 throughout the domain, and the streamwise (Δx^+) and cross-stream (Δy^+) grid sizes near the endwall were reduced to a value of approximately 25, based on the inlet boundary layer friction velocity. Triangular cells were used to mesh the endwall face, and were extruded normal to that face along the airfoil span with an inflation ratio of 1.15 to construct prismatic cells. Because of computational resource limitations, the spanwise spacing away from the endwall was increased so that Δz^+ was approximately 85 near the symmetry plane. The overall mesh size was 44 million cells, with the majority concentrated near the endwall. Figure 2 depicts the mesh at various locations around the domain.

An unsteady inlet velocity field was generated using the spectral synthesizer available in Fluent, which is based on the random flow generation technique of Smirnov et al. [44]. A divergence-free velocity field is synthesized from random variation of 100 Fourier harmonics and added to the mean velocity. This method requires realistic velocity, turbulent kinetic energy, and specific dissipation profiles from a RANS solution to produce realistic “eddies”. In this study, the RSM model (which extended further upstream than the LES domain) was used to generate the inlet profiles for the spectral synthesizer. The mean temperature profile from the RSM model was also used as an input to the LES model, although no capability for unsteady inlet temperature fluctuation is currently available in Fluent.

The LES model was solved in Ansys Fluent, version 18 using the dual-time-stepping approach, with 30 subiterations per

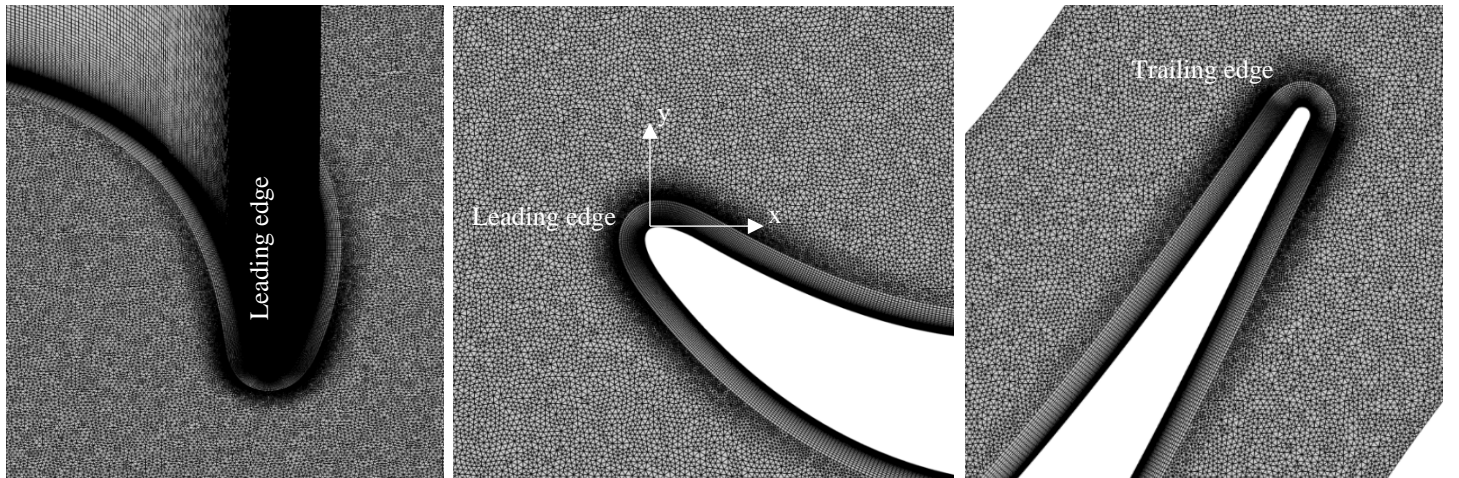


Figure 2. Computational mesh for LES model.

timestep. These many subiterations were generally sufficient to reduce the residuals by 4 orders of magnitude. Spatial gradients of pressure and temperature (energy equation) were discretized using second-order upwinding, and momentum terms were discretized using bounded central differencing (essentially second-order accurate). Temporal derivatives were calculated using a bounded second-order implicit formulation. To ensure CFL numbers of 1 or lower through the domain, the timestep was set at 2×10^{-5} sec, which corresponds to a nondimensional value of $\Delta t * U_{in}/C_{ax} = 7.8 \times 10^{-4}$ based on domain inlet velocity and blade axial chord, or $\Delta t * u_{\tau}^2/\nu = 0.14$ based on the friction velocity at $1.0C_{ax}$ upstream of the blade. The instantaneous solution was initialized from a steady solution and run for approximately two flow-through times before beginning data sampling. Approximately eight flow through times were captured after data sampling was activated. The inlet boundary layer mean and RMS velocity profile, the spatial distribution of the time-mean endwall heat transfer coefficient, and the time-mean and RMS velocity field at the cascade exit were compared between the sixth and eighth flow through times and exhibited small variations indicating temporal convergence. For example, the mean x-velocity varied by less than 0.9%, and the RMS x-velocity varied by less than 2%, in the passage vortex core location at $1.03C_{ax}$ downstream of the leading edge plane.

VALIDATION

The measured inlet boundary layer profiles at $1.0C_{ax}$ upstream of the blade inlet plane are compared to the two computational models in Figure 3. The mean velocity magnitude (two-component, based on u and v) is plotted in both outer coordinates based on boundary layer thickness and freestream velocity, as well as on inner coordinates based on friction velocity. The turbulent kinetic energy profile is also shown, in inner coordinates. The RSM model agrees very well to the experimental data for the mean velocity profile, and also reasonably predicts the turbulent kinetic energy profile in the boundary layer, but dramatically overpredicts the turbulence in the freestream. The cause of this is not exactly clear, but the determination of the turbulence length scale in the RSM model is based on the $k - \omega$ formulation, which has known sensitivity to freestream boundary conditions. Unfortunately a dissipation boundary condition is not available from the experiments. The mean velocity profile from the LES model shows a similar trend to the experiments, but has some slight deviation probably due to a development length that is not quite sufficient to establish the same boundary layer maturity as the RSM model. Also, the fall-off of the turbulent kinetic energy in the log region of the boundary layer is more rapid for the LES model than observed in the experiment. This unfortunately may be due to the switch between the RANS-dominated zone right near the wall, and the LES-dominated zone away from the wall, which may need to be refined (although outside the scope of this work). However, the prediction of the freestream k from the LES model matches well to the experiment.

Table 1 compares the computed inlet boundary layer parameters at $1.0C_{ax}$ upstream to the experiment of Lynch [45].

Both computational models predict smaller boundary layer thicknesses and momentum thickness Reynolds numbers than in the experiment, which may have a slight impact on the development of the secondary flow in the blade passage.

The airfoil midspan nondimensional static pressure as a function of surface distance from the airfoil leading edge is

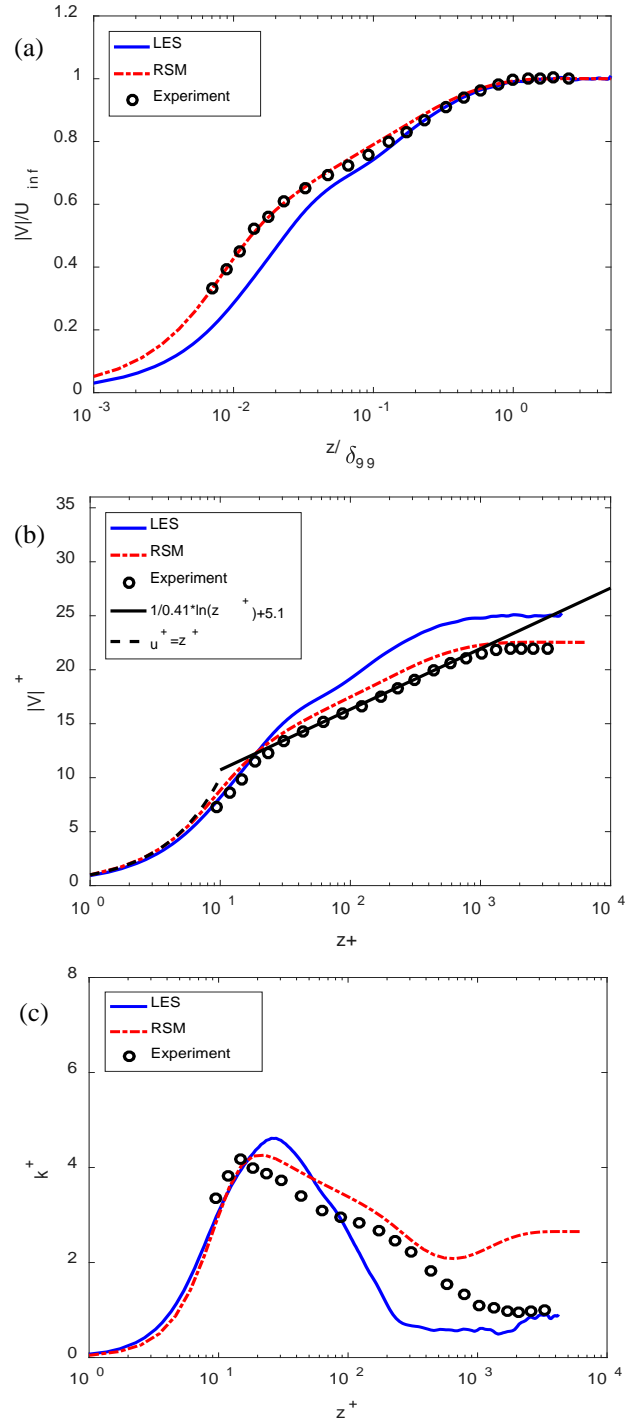


Figure 3. Comparisons of the predicted boundary layer at $x/C_{ax} = -1.0$ to the experiment of Lynch et al. [45].

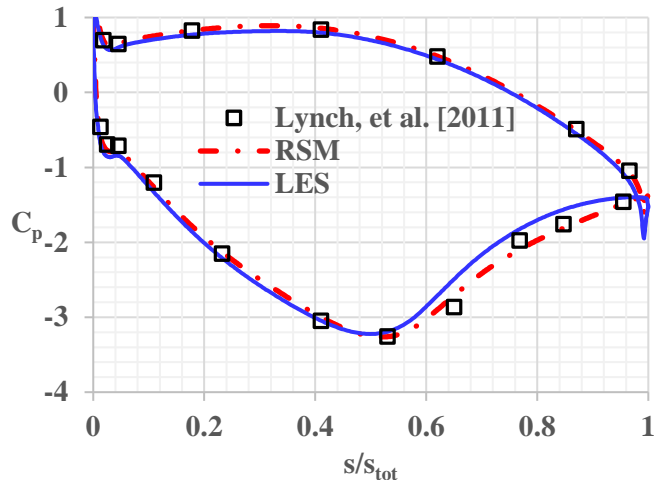


Figure 4. Static pressure coefficient at midspan compared to Lynch et al [45].

shown in Figure 4 for the experiment and the two models. In general, there is very good agreement over most of the airfoil surface, with some deviation on the aft suction side beyond $s/s_{tot}=0.6$. A closer inspection of the suction side flowfield at midspan can be seen in Figure 5. Here, it is clear that the wake of the airfoil for the LES model is larger than for the RSM model. The reasons for this are not exactly clear, but the large spanwise grid spacing near midspan may result in under-resolution of the suction side boundary layer; also, the LES model tended to damp out freestream turbulence in the blade passage, which normally would trigger transition to a turbulent boundary layer.

Table 1: Inlet boundary layer parameters at $x/C_{ax}=-1.0$

Variable	Experiment [45]	RSM	LES
U_{in} [m/s]	8.51	8.58	8.61
u_r [m/s]	0.388	0.381	0.344
δ_{99} [mm]	53.5	48.7	39.9
θ [mm]	3.7	3.2	3.0
Re_θ	2004	1679	1576
Tu	4.9%	5.9%	4.4%

RESULTS

A qualitative description of the cascade secondary flow features predicted by the LES model is first described, followed by comparisons of endwall shear and heat transfer. The flowfield comparisons include both planes in the passage, as well as detailed boundary layer profiles of mean and fluctuating velocity components.

Overall Flowfield

To visualize endwall flow structures, an isosurface of q -criterion was computed at a time instant from the LES model. q -criterion is the second invariant of the velocity gradient tensor [46], and is a commonly used metric to identify turbulent features. Figure 6 shows several views of the cascade, with isosurfaces of q -criterion colored by instantaneous velocity

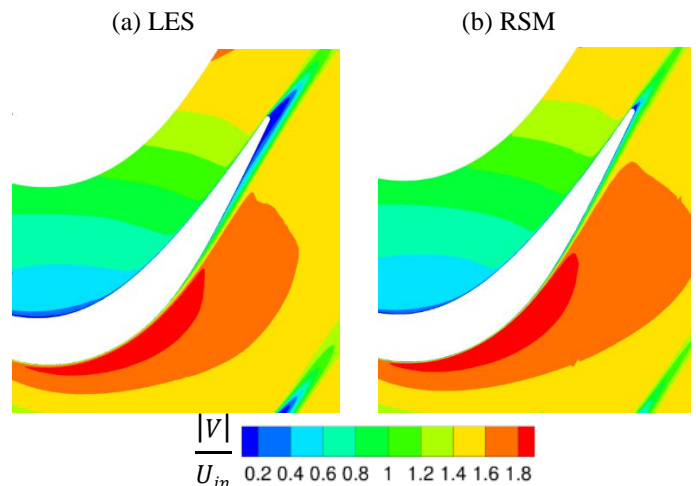


Figure 5. Time-average suction side flowfield at midspan, showing thicker suction side boundary layer for LES.

magnitude. The value for the q -criterion isosurface level ($q=50,000$) was selected to best depict the vortex structures in the incoming boundary layer as well as the wake shedding from the airfoil trailing edge. The canonical hairpin vortex structures of a turbulent boundary layer are present upstream of the cascade and are randomly distributed. Just into the passage, the structures are turned by the pitchwise pressure gradient and appear to be elongated in the direction of the endwall secondary flow from pressure to suction side. This aligns the hairpin vortices with the flow direction, which might be expected to significantly change the nature of the turbulence. Several of the vortices are bundled up into a larger swirling structure which is the passage vortex that moves toward the minimum pressure point on the suction side, and then climbs along the suction side of the blade. Further into the passage, there is a noticeable lack of turbulent vortex structures, which could be due to the choice of the q -criterion level but is consistent with the understanding that this region may have a laminar-like boundary layer developing on the endwall downstream of the passage vortex. The back view of the cascade shows the merger of the passage vortex with the regular wake shedding from the airfoil trailing edge. At the time of this writing there was not enough data to determine if the secondary flow “synchronizes” to the airfoil wake shedding, but this is an interesting point that has not previously received attention, to the author’s knowledge.

Endwall Shear and Heat Transfer

The experiment of Lynch [12] included an oil flow visualization of the endwall flow, which is compared to the computational models in Figure 7. The experimental result was low contrast, so nominal streaklines were drawn to emphasize the wall shear pattern. It should be noted that the accuracy of oil flow visualization in indicating endwall flow direction can be suspect around three-dimensional separations, but is considered a reasonable approximation. For the computational models, the quantitative friction coefficient is shown in contours, and endwall streaklines are determined by the wall shear vector

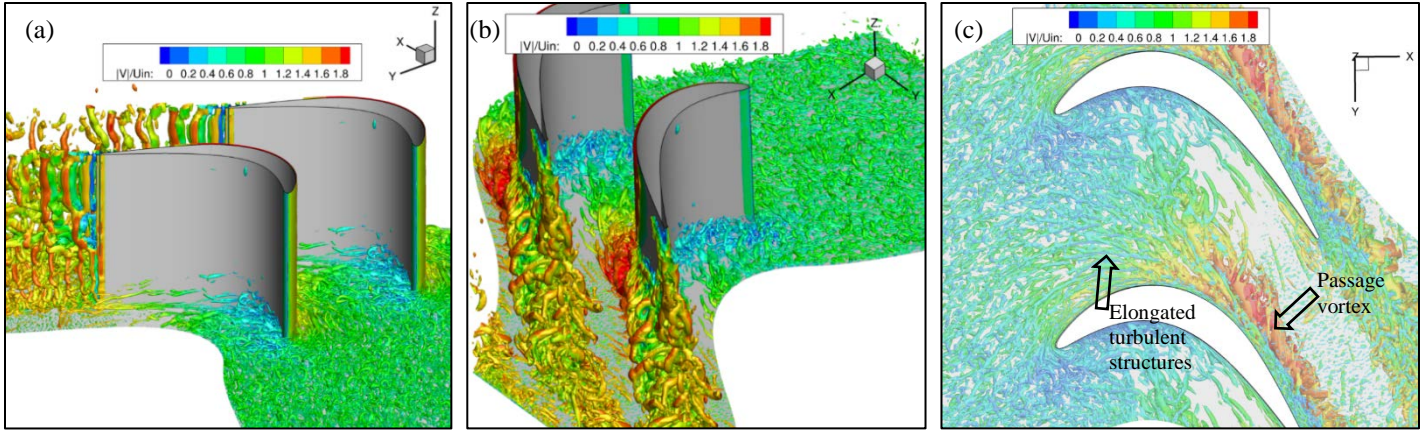


Figure 6. Instantaneous isosurfaces of q -criterion for (a) forward view, (b) aft view, and (c) under-endwall view (transparent endwall).

directions and seeded in approximately the same locations as the experimental streaklines. In the experiment, there is a clear region upstream of the airfoil leading edge that is the incoming endwall separation (saddle point). The saddle point is associated with zero friction in the computational studies, and both cases indicate good agreement in its location upstream of the leading edge. There is also a cleared region in Figure 7a which is most

likely a low shear region caused by the upwash of the passage vortex. During the experiment, the oil pooled along this line and was swept downstream. In the computations, this appears as a kink in the endwall shear contours. The kink appears to be slightly further into the passage than indicated by the experiment, although the lack of comparable measurements (oil flow versus endwall friction coefficient) limits the interpretation.

Both computational models indicate high shear near the suction side, around the minimum flow area (“throat”) in the passage. At this point, the passage vortex is large but close to the endwall and causes high scraping velocity. Further downstream along the suction side, the separation line moves slightly away from the airfoil-endwall junction due to the growth of a small suction side corner vortex as well as the displacement of the passage vortex away from the wall. One of the more significant but subtle differences between the RSM and LES models is the wall shear right at the suction side airfoil-endwall corner close to the trailing edge. The RSM result in Figure 7b indicates low wall shear due to separated flow under the passage vortex. However the LES model in Figure 7c shows a thin band of high friction coefficient. An instantaneous snapshot of the wall shear in Figure 7d gives a possible explanation for this difference. A significant variation in instantaneous shear levels is seen along the aft suction side-endwall junction, which would manifest as high unsteadiness and increase the local shear relative to the steady separated flow predicted by the RSM model.

Nondimensional endwall heat transfer predictions (presented as St number based on inlet velocity) are compared to the experiment of Lynch, et al. [12] in Figure 8. The white dashed line overlaid on the experimental results is an inviscid streamline passing through the midpitch of the passage at the leading edge plane, and is used to extract direct comparisons in Figure 9. In Figure 8, there are several important features of the endwall heat transfer that are generally captured. First, the predictions indicate high heat transfer at the airfoil-endwall junction in the lee of the pressure side, as seen in the experiment. Also, heat transfer levels are high around the trailing edge. However, both computational models indicate higher heat transfer midway into the passage than seen in the experiment.

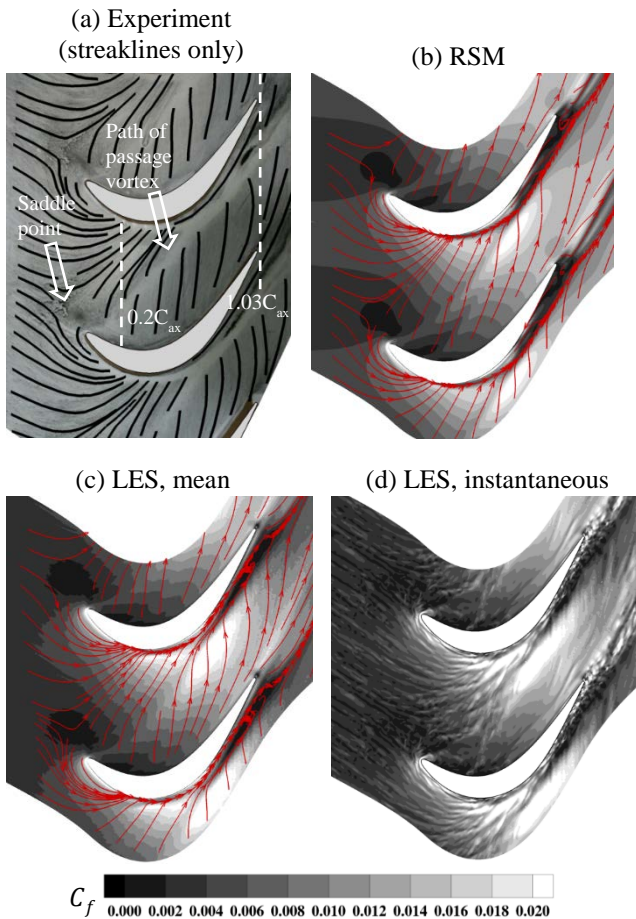


Figure 7. (a) Endwall oil flow from the experiments of Lynch et al. [12], compared to endwall shear predictions.

The steady RSM model clearly predicts sharp gradients around the passage vortex path, which are smoothed out in the LES results due to overall unsteadiness of that flow. As was seen in the friction results, the RSM model predicts low heat transfer all along the aft suction side, whereas the LES model has increased heat transfer (more similar to the experiment) on the suction side

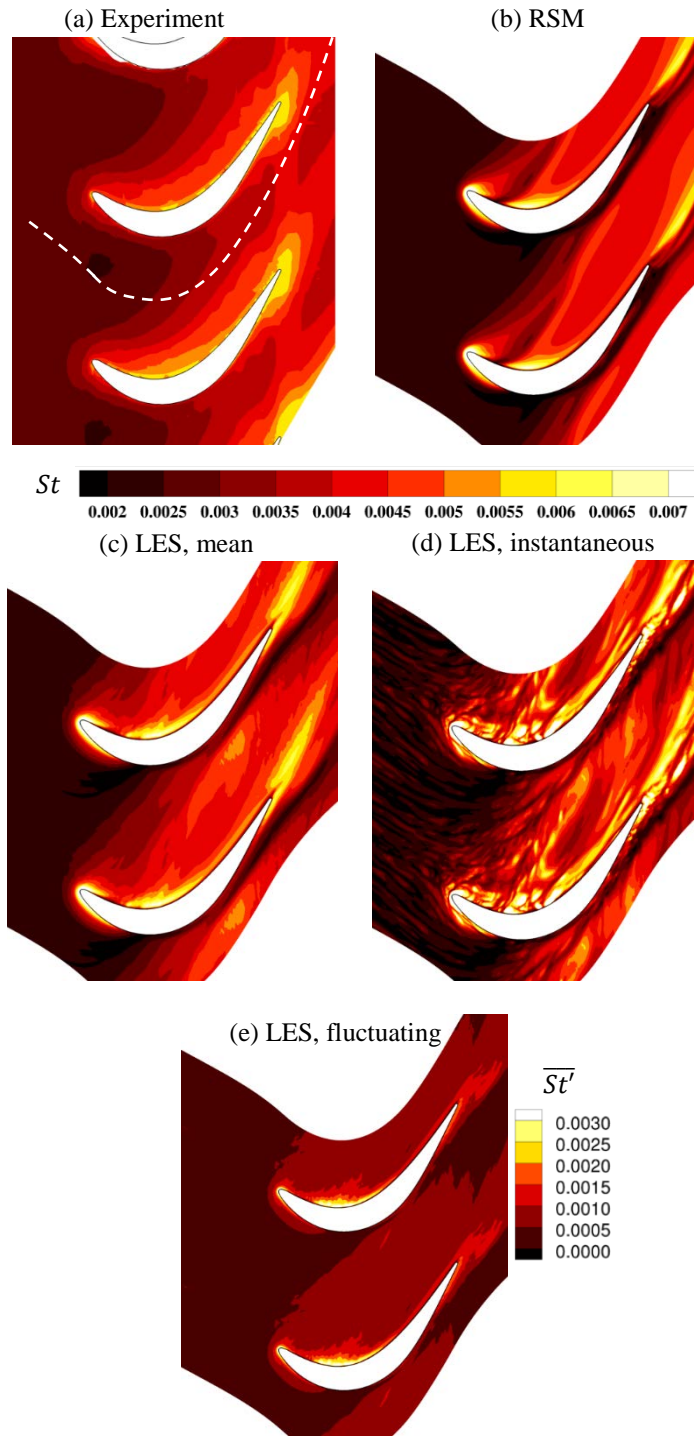


Figure 8. Endwall heat transfer from experiment of Lynch, et al. [12], compared to predictions.

trailing edge due to flow unsteadiness. Finally, both models overpredict the persistence of high heat transfer in the wake of the airfoil, relative to the experiment.

Figure 8d and e provide some unique information about the unsteadiness of the heat transfer in endwall secondary flows. There is significant spatial variation of the instantaneous heat transfer near the lee of the pressure side where mean heat transfer is high; the impact of this is reflected in the RMS of the fluctuating heat transfer, which is highest at that point of the endwall. In fact, the RMS of the fluctuation is up to 38% of the mean heat transfer. Even in the middle of the passage, fluctuations can be 20% of the mean heat transfer value, due to secondary flow unsteadiness.

A quantitative comparison of mean heat transfer along the path in Figure 8a, where the abscissa is x-coordinate normalized by axial chord, is shown in Figure 9. Also included is the variation in heat transfer from the LES result, where the local RMS fluctuation level is added to the local mean value. The computations slightly underpredict the incoming surface heat transfer relative to the experiment, due to the differences in the approach momentum and thermal boundary layer thicknesses. Both the LES and the RSM model predict higher heat transfer in the passage between 0.4-1.1 C_{ax} . This is approximately the region where the incoming turbulent boundary layer separates and there is a distinct lack of turbulent vortex structures in Figure 6c. If this region is truly a laminar flow region, then the turbulence modeling approaches of the RSM and the wall-modeled LES may not be able to adequately predict the heat transfer. Or, note that both models still use the Reynolds analogy to determine the turbulent heat flux in the near-wall region. It is not clear that the gradient diffusion hypothesis, or a singular value of turbulent Prandtl number, is appropriate in this region of highly three-dimensional, laminar-like flow.

Passage Flowfield Comparisons

Mean and turbulent flowfield measurements were obtained with a laser Doppler velocimeter at two axial planes in the study of Lynch and Thole [41] and Lynch [29]. The axial planes are

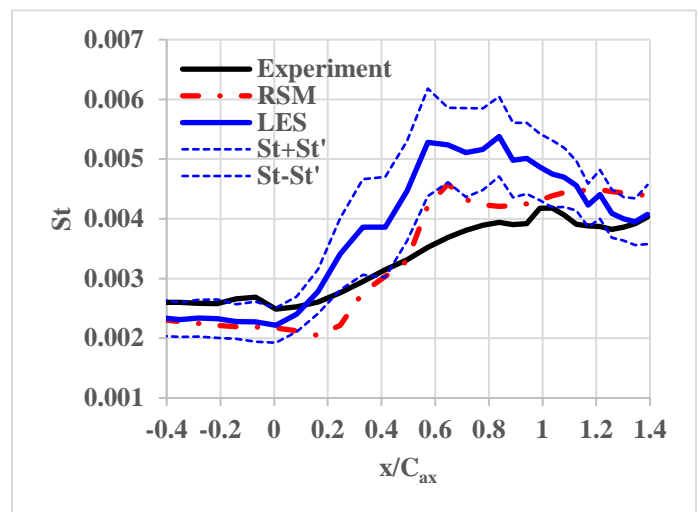


Figure 9. Heat transfer extracted along pathline in Fig. 8.

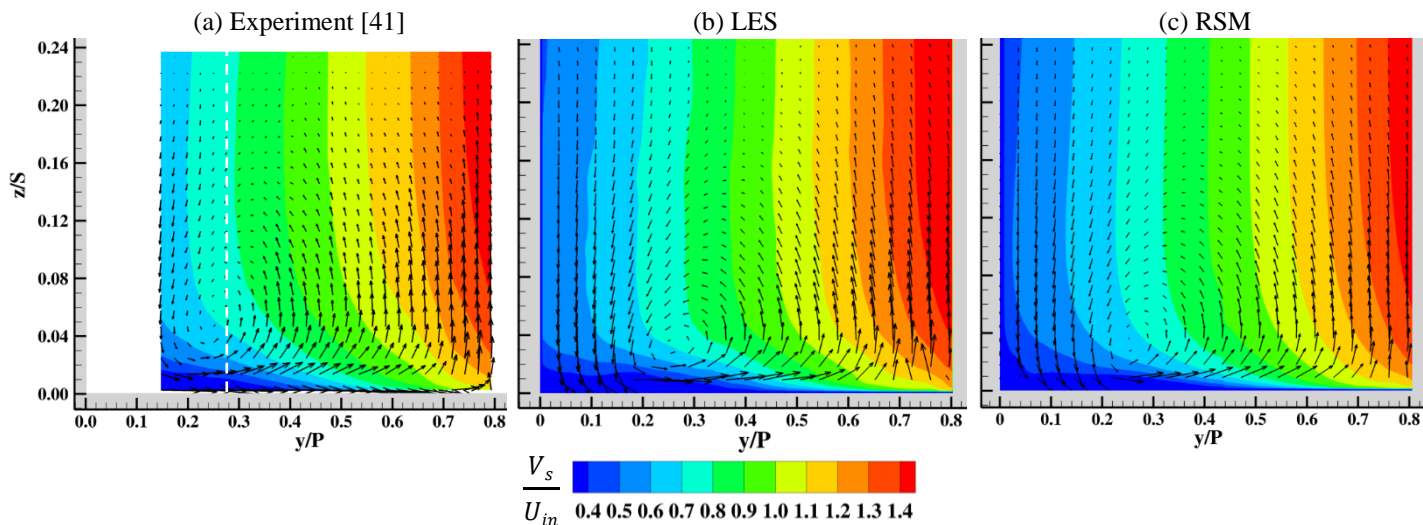


Figure 10. Mean secondary flow vectors overlaid on contours of mean streamwise velocity.

located at $0.2C_{ax}$ and $1.03C_{ax}$ from the leading edge plane (see Figure 7), to capture the initial development of the secondary flow and the nearly-complete development as it exits the blade passage. In addition, detailed boundary layer traverses were performed at discrete locations within these planes to capture the near-wall behavior around the secondary flow.

For a given pitchwise location in a measurement plane, the velocity in x - y - z coordinates is transformed into a coordinate system aligned with the local inviscid flow direction (obtained at midspan). Then, vectors are plotted with velocity components normal to this direction (V_n) and aligned with the span direction (V_z), which more clearly show the secondary flow not aligned with the inviscid flow direction. Figure 10 shows a comparison of the secondary flow vectors overlaid on contours of streamwise velocity. Note that the experimental measurements do not quite cover the passage due to optical access limitations. Also, the white dashed line on the figure indicates the location of an endwall boundary layer profile described later in Figure 12.

There is generally good agreement in streamwise velocity magnitude and secondary flow pattern between the measurements and predictions in Figure 10, but some important distinctions are noted. First, the measured position of the passage vortex core (as determined by the center of the swirling feature) is at $y/P=0.25$, whereas both models predict the core to be at $y/P=0.28$. This explains the slight differences in the passage vortex trajectories, and the subsequent differences in endwall heat transfer, observed earlier. Also, the vortex core is further from the endwall; $z/S=0.05$ for the experiment versus $z/S=0.03$ for the models.

Normalized turbulent kinetic energy (k) at $0.2C_{ax}$, overlaid with time-average secondary flow vectors, is shown in Figure 11. The high fluctuations under the time-average position of the passage vortex are manifested as high k levels. There is more discrepancy between the measurements and the predictions in this figure, with the measurements indicating high levels of turbulence broadly distributed over the endwall. The RSM model

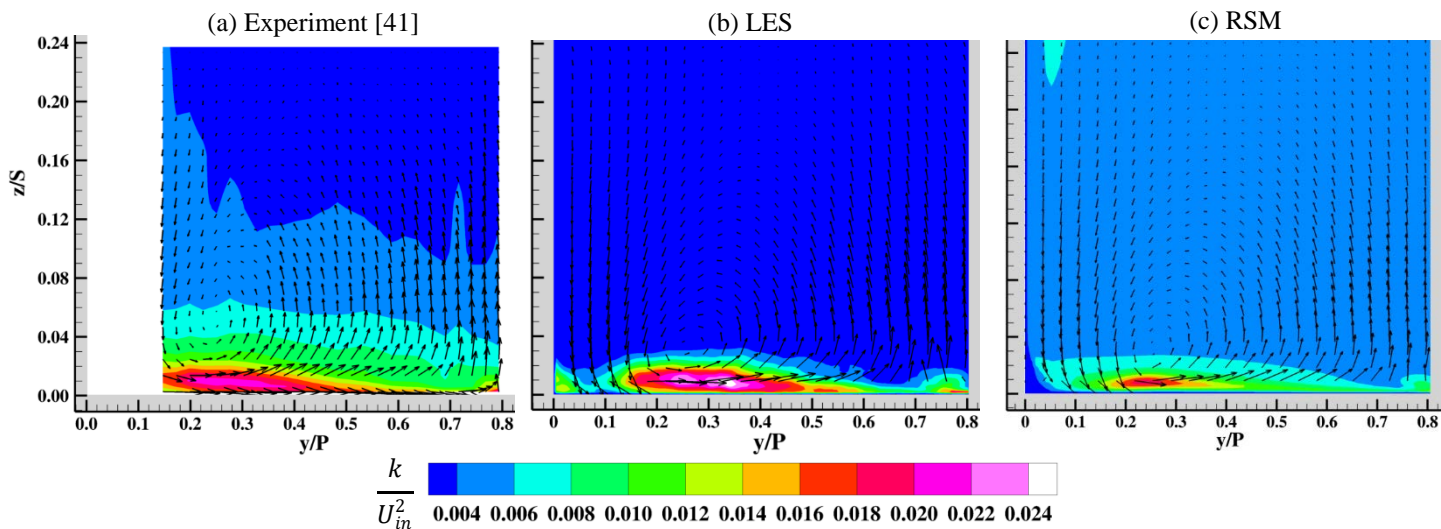


Figure 11. Contours of turbulent kinetic energy overlaid with mean secondary velocity vectors.

also shows a distribution of k , but the turbulence associated with the passage vortex is very concentrated. The LES model slightly overpredicts the peak k but generally gets the distribution under the vortex core correct. Examination of successive snapshots of the instantaneous velocity (not shown) indicates wandering of the passage vortex along the endwall, which results in the broad distribution of k . In addition, the LES model resolves the high k in the suction side vortex on the right side of the plane.

Boundary layer profiles of mean and fluctuating velocities were obtained along the white dashed line in Figure 10a, and are plotted using inner coordinate scaling in Figure 12. Note here that the velocities are in the blade cascade coordinate system (u, v, w) . The predictions of the mean u -velocity (u^+) and v -velocity (v^+) show reasonable agreement between the models and the experiment, except perhaps for the LES model which predicts a slightly lower u^+ in the freestream. However, there are some interesting discrepancies in the normal Re stress terms in Figure 12c. There are particularly high $\overline{u'u'^+}$ and $\overline{v'v'^+}$ values around a z^+ of 100, which are associated with the high k levels of the passage vortex discussed earlier. The RSM model does not

distinguish a difference between the peak u and v fluctuations, but gets the peak $\overline{v'v'^+}$ values correct and underpredicts the $\overline{u'u'^+}$ peak. The LES model predicts more anisotropy in the Re normal stresses than the RSM model, but does not predict the peak values or even the correct relative ranking. Both models seem to reasonably predict the Re shear stresses associated with the u -direction fluctuations ($\overline{u'v'^+}, \overline{u'w'^+}$), but overpredict the Re stress associated with the cross-stream-wall-normal fluctuations ($\overline{v'w'^+}$). This stress is related to the turbulent actions of the hairpin vortex structures being turned toward the suction side by the cross-passage pressure gradient (see Figure 6c). As found by other researchers [47, 48], this significant flow three-dimensionality can impair the ability of the hairpin structures in generating turbulence.

Figure 13 shows secondary flow vectors and contours of streamwise velocity for the exit plane at $1.03C_{ax}$. The wakes of the airfoils are visible as low-streamwise velocity regions, and the passage vortex is now a larger feature toward the right of the figures. The black dashed line indicates the projected trailing

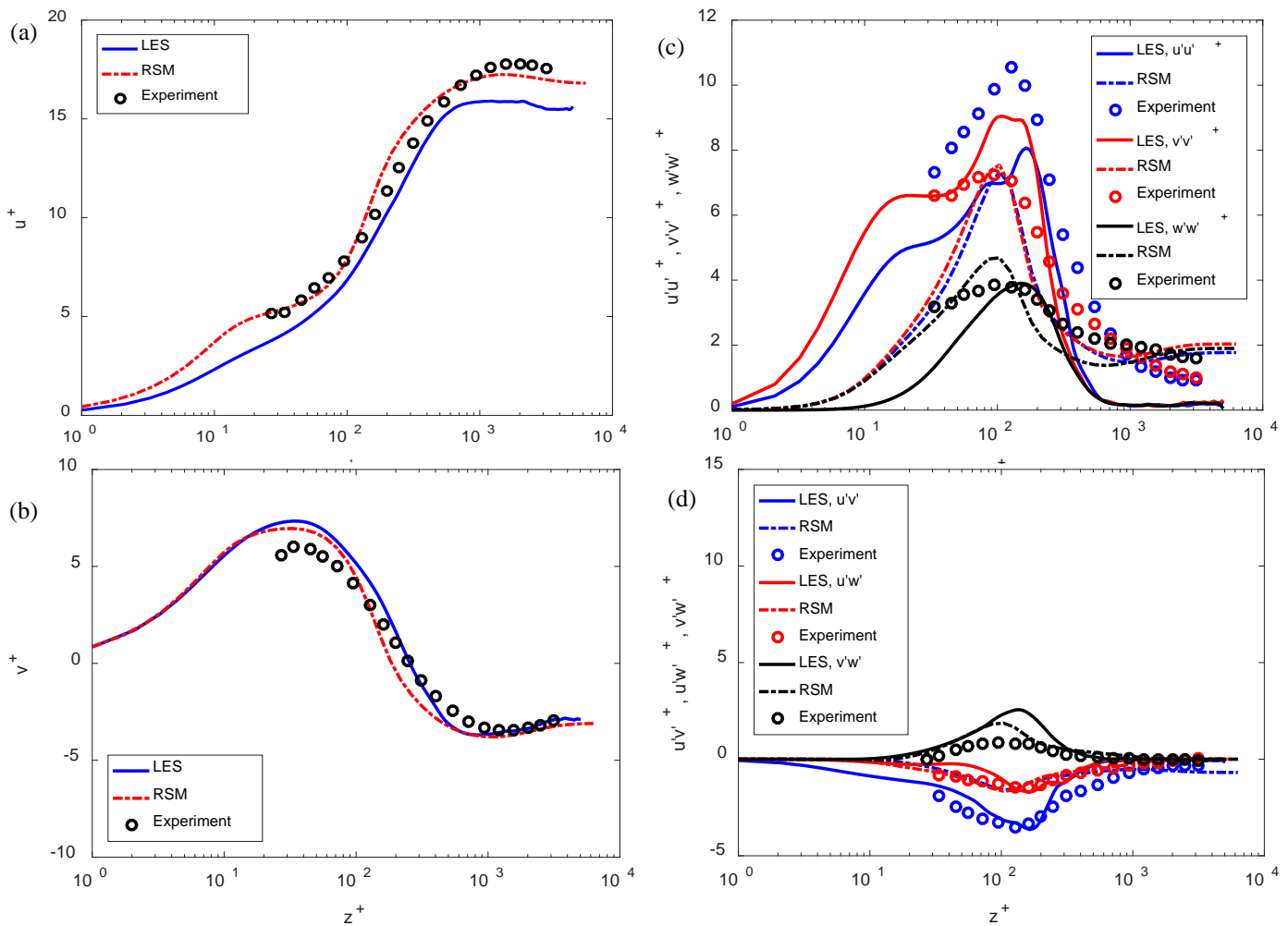


Figure 12. Boundary layer profiles along the white line in Fig. 10a, for Lynch [29] and the computational models.

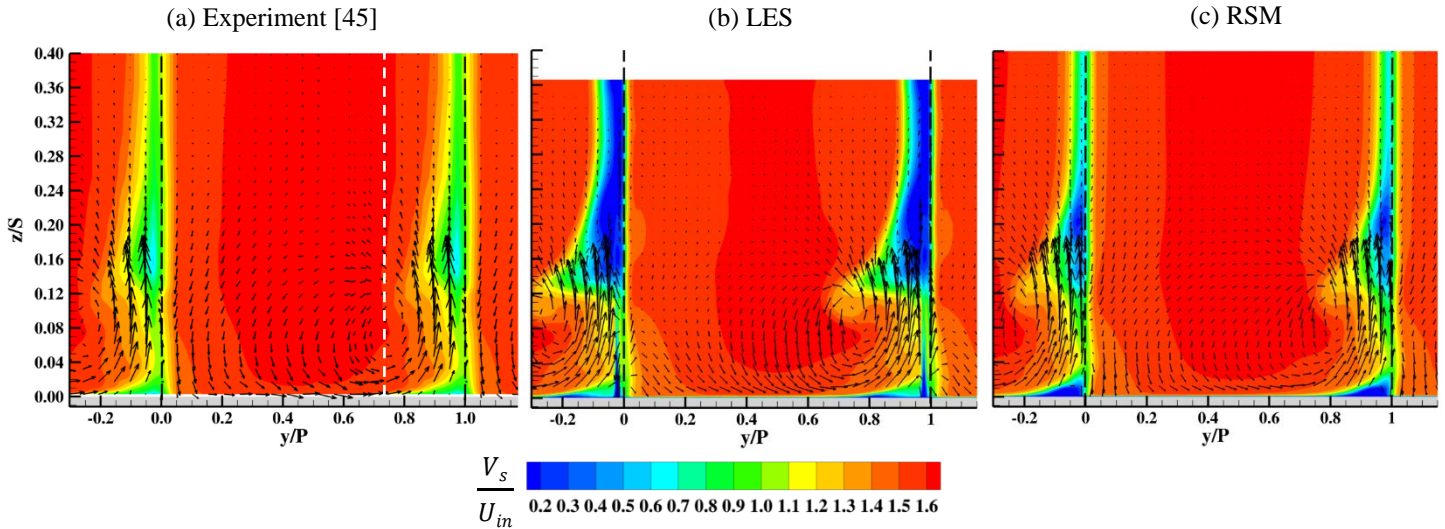


Figure 13. Mean secondary velocity vectors overlaid on mean streamwise velocity contours at $x/C_{ax}=1.03$.

edge location of the airfoil along the inviscid flow direction; the region to the left of a black dashed line is the airfoil suction side and the region to the right is associated with the pressure side. The white dashed line is the location for boundary layer profiles described in Figure 15.

Figure 13 shows less satisfactory agreement between the various modeling cases and the experiment with regards to streamwise velocity magnitude, with underprediction in the secondary flow region and the airfoil wake, even at midspan. As described earlier, the suction side boundary layer in the LES model is thicker than expected from the experiment, although it should be noted that this analysis plane is located in a region of high streamwise gradients right near the trailing edge and slight variation in position can impact the conclusions. The LES model seems to get the position of the time-average passage vortex core reasonably well, but the RSM model passage vortex is too far toward the suction side relative to the experiment. Another area

where the LES prediction is better than the RSM is near the suction side airfoil-endwall corner at $y/P=0.8-1.0$. As previously discussed, the unsteadiness in this region is better captured by the LES approach.

Normalized turbulent kinetic energy contours with overlaid time-mean secondary flow in Figure 14 actually indicate an overprediction of k near the suction side-endwall corner for the LES model relative to the experiment. In contrast, the RSM model significantly underpredicts k in that region which explains the poor prediction of friction and heat transfer described earlier. The LES model also overpredicts peak k in the strong spanwise-oriented vectors at the edge of the passage vortex; secondary flow theory for turbines suggests that this region contains some of the suction side airfoil boundary layer fluid entrained by the passage vortex. The overprediction of the suction side boundary layer thickness in the LES model likely contributes to the high k seen here.

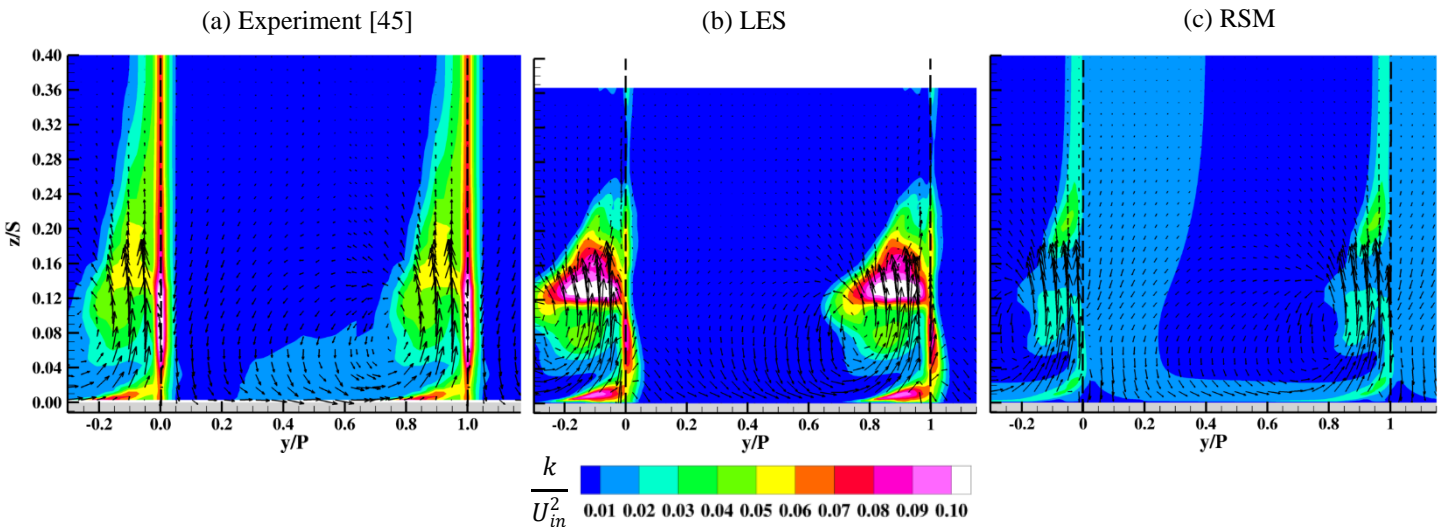


Figure 14. Turbulent kinetic energy contours overlaid with mean secondary velocity vectors at $x/C_{ax}=1.03$.

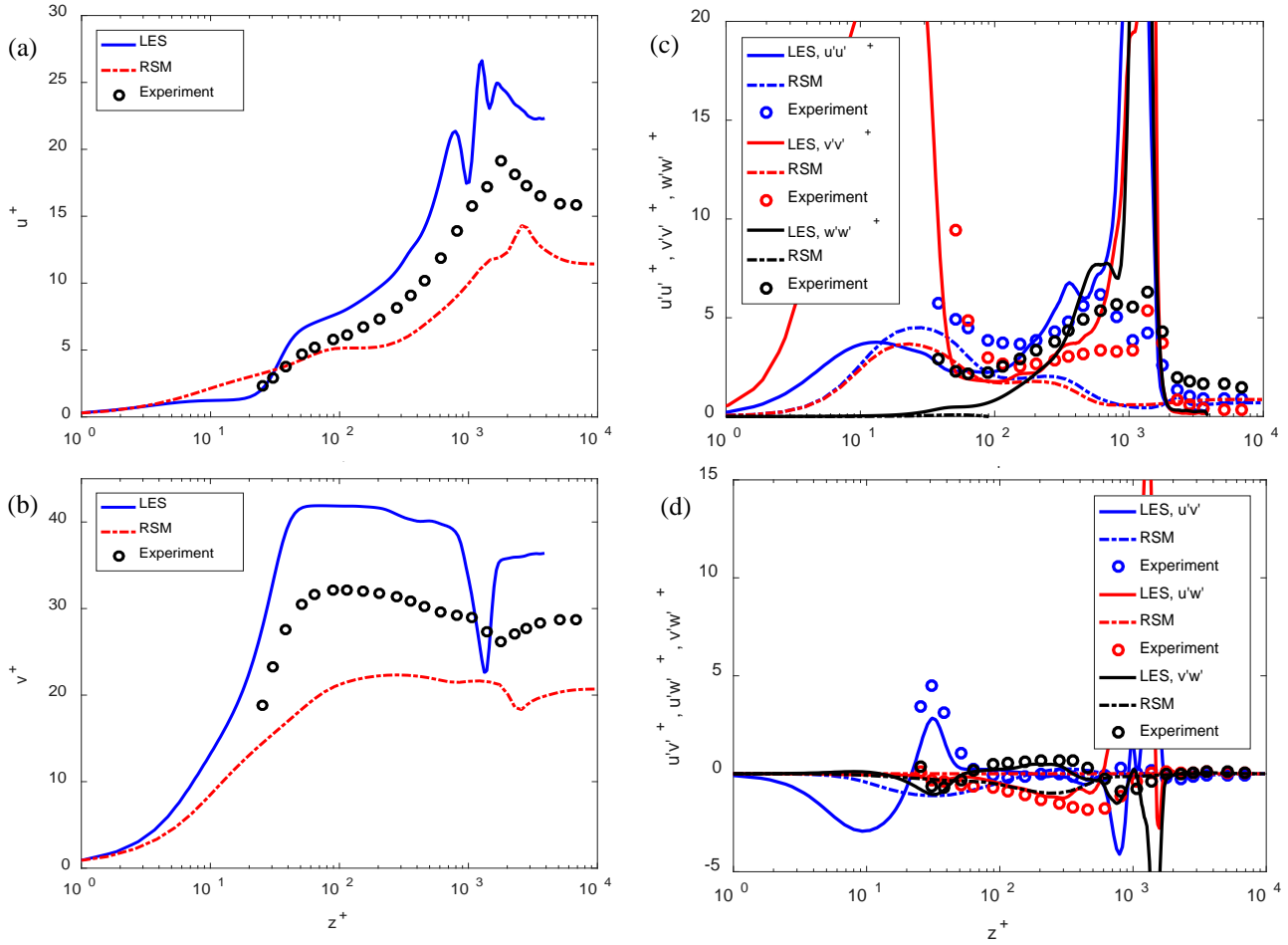


Figure 15. Boundary layer profiles along the white line in Fig. 13, for the experiment of Lynch [29] and the computational models.

Boundary layer mean and fluctuating velocity profiles are extracted at the location indicated by the white dashed line in Figure 13 and compared to the experiment in Figure 15. The coordinates are again based on the cascade coordinate system and results are normalized using inner coordinates. Although the magnitudes of u^+ and v^+ are very different between the various models, this is an artifact of different friction velocity values at this location. The RSM model overpredicts friction velocity (resulting in low u^+ and v^+), while the LES model underpredicts friction velocity. Reynolds normal stress terms in Figure 15c are not so well predicted by either model, although the trend of high $\overline{v'v'^+}$ below $z^+=30$ seems to somewhat follow the experiment (no data was possible below that z^+). Reynolds shear stresses are moderately well predicted by the LES model below $z^+=700$, even showing the small peak in $\overline{u'v'^+}$ at $z^+=30$. These would be correlations between fluctuations in a plane parallel to the wall, possibly associated with wandering of the passage vortex which is right above this location.

CONCLUSIONS

This study presented comparisons of a steady Reynolds stress model (RSM) and a wall-modeled large eddy simulation (LES) model to experimental measurements of endwall heat transfer and mean/turbulent flow in a low pressure turbine cascade. The LES model did not improve predictions of time-average heat transfer, but did indicate the importance of modeling the unsteady nature of secondary flow which cannot be predicted in a steady approach. Turbulence quantities in the forward part of the passage were better predicted by LES than RSM, but were overpredicted toward the exit of the passage due to an artificially thick suction side boundary layer in the LES model.

More work remains to determine which specific model features in the LES are responsible for the misprediction of endwall heat transfer. Certainly the high skew in a turbine blade passage is difficult for wall-modeling approaches to capture, since the turbulence is significantly anisotropic. A more careful dataset with detailed measurements throughout the developing skewed turbulent boundary layer, as well as in the laminar-like

or transitional region downstream of the passage vortex, is recommended.

Future work should consider the total pressure losses from the LES approach, and investigate ways to reduce the thickened suction side boundary layer so that the midspan wake measurements more closely match the experiment. Also, any temporal alignment between the horseshoe vortex breakdown, aft suction side corner flow, and the wake shedding frequency should be investigated in more detail.

ACKNOWLEDGMENTS

The author would like to acknowledge the use of the Penn State Advanced Cybercomputing Infrastructure (PSU-ACI) for the high performance computing presented here, as well as the prior advice and assistance of Dr. Atul Kohli and Dr. Karen Thole regarding the experimental results.

REFERENCES

- [1] Langston, L. S., Nice, M. L., and Hooper, R. M., 1977, "Three-Dimensional Flow Within a Turbine Cascade Passage," *J. Eng. Power*, 99, pp. 21-28.
- [2] Langston, L. S., 1980, "Crossflows in a Turbine Cascade Passage," *J. Eng. Power*, 102, pp. 866-874.
- [3] Horlock, J. H., and Lakshminarayana, B., 1973, "Secondary Flows: Theory, Experiment, and Application in Turbomachinery Aerodynamics," *Ann. Rev. Fluid Mech.*, 5(1), pp. 247-280.
- [4] Sieverding, C. H., 1985, "Recent Progress in the Understanding of Basic Aspects of Secondary Flows in Turbine Blade Passages," *J. Eng. Gas Turbines Power*, 107(2), pp. 248-257.
- [5] Sharma, O. P., and Butler, T. L., 1987, "Predictions of Endwall Losses and Secondary Flows in Axial Flow Turbine Cascades," *J. Turbomach.*, 109(2), pp. 229-236.
- [6] Gregory-Smith, D. G., 1982, "Secondary Flows and Losses in Axial Flow Turbines," *J. Eng. Power*, 104(4), pp. 819-822.
- [7] Coull, J. D., 2017, "Endwall Loss in Turbine Cascades," *J. Turbomach.*, 139(8), pp. 081004-081004-081012.
- [8] Graziani, R. A., Blair, M. F., Taylor, J. R., and Mayle, R. E., 1980, "An Experimental Study of Endwall and Airfoil Surface Heat Transfer in a Large Scale Turbine Blade Cascade," *J. Eng. Power*, 102(2), pp. 257-267.
- [9] Kang, M. B., Kohli, A., and Thole, K. A., 1999, "Heat Transfer and Flowfield Measurements in the Leading Edge Region of a Stator Vane Endwall," *J. Turbomach.*, 121(3), pp. 558-568.
- [10] Gaugler, R. E., and Russell, L. M., 1984, "Comparison of Visualized Turbine Endwall Secondary Flows and Measured Heat Transfer Patterns," *J. Eng. Gas Turbines Power*, 106, pp. 168-172.
- [11] Giel, P. W., Thurman, D. R., Fossen, G. J. V., Hippensteele, S. A., and Boyle, R. J., 1998, "Endwall Heat Transfer Measurements in a Transonic Turbine Cascade," *J. Turbomach.*, 120(2), pp. 305-313.
- [12] Lynch, S. P., Sundaram, N., Thole, K. A., Kohli, A., and Lehane, C., 2011, "Heat Transfer for a Turbine Blade With Nonaxisymmetric Endwall Contouring," *J. Turbomach.*, 133(1), pp. 011019-011019.
- [13] Laveau, B., Abhari, R. S., Crawford, M. E., and Lutum, E., 2014, "High Resolution Heat Transfer Measurements on the Stator Endwall of an Axial Turbine," *J. Turbomach.*, 137(4), pp. 041005-041005.
- [14] Benton, S. I., Bons, J. P., and Sondergaard, R., 2012, "Secondary Flow Loss Reduction Through Blowing for a High-Lift Front-Loaded Low Pressure Turbine Cascade," *J. Turbomach.*, 135(2), pp. 021020-021020.
- [15] Thrift, A. A., and Thole, K. A., 2012, "Influence of flow injection angle on a leading-edge horseshoe vortex," *Int. J. Heat Mass Transfer*, 55(17-18), pp. 4651-4664.
- [16] Zess, G. A., and Thole, K. A., 2002, "Computational Design and Experimental Evaluation of Using a Leading Edge Fillet on a Gas Turbine Vane," *J. Turbomach.*, 124(2), pp. 167-175.
- [17] Mahmood, G. I., and Acharya, S., 2007, "Experimental Investigation of Secondary Flow Structure in a Blade Passage With and Without Leading Edge Fillets," *J. Fluids Engr.*, 129(3), pp. 253-262.
- [18] Saha, A. K., Mahmood, G. I., and Acharya, S., 2006, "The Role of Leading-Edge Contouring on End-Wall Flow and Heat Transfer: Computations and Experiments," *Proc. ASME Turbo Expo 2006*, Paper GT2006-91318.
- [19] Knezevici, D. C., Sjolander, S. A., Praisner, T. J., Allen-Bradley, E., and Grover, E. A., 2010, "Measurements of Secondary Losses in a Turbine Cascade With the Implementation of Nonaxisymmetric Endwall Contouring," *J. Turbomach.*, 132(1), p. 011013.
- [20] Laveau, B., Abhari, R. S., Crawford, M. E., and Lutum, E., 2013, "High Resolution Heat Transfer Measurement on Flat and Contoured Endwalls in a Linear Cascade," *J. Turbomach.*, 135(4), pp. 041020-041020.
- [21] Lyall, M., Clark, J., King, P., and Sondergaard, R., 2013, "End Wall Loss Reduction of High Lift Low Pressure Turbine Airfoils Through Use of Profile Contouring—Part I: Airfoil Design," *Proc. ASME IGTI Turbo Expo*, Paper GT2013-95000.
- [22] Praisner, T. J., Allen-Bradley, E., Grover, E. A., Knezevici, D. C., and Sjolander, S. A., 2013, "Application of Nonaxisymmetric Endwall Contouring to Conventional and High-Lift Turbine Airfoils," *J. Turbomach.*, 135(6), pp. 061006-061006.
- [23] Sangston, K., Little, J., Lyall, M. E., and Sondergaard, R., 2014, "End Wall Loss Reduction of High Lift Low Pressure Turbine Airfoils Using Profile Contouring—Part II: Validation," *J. Turbomach.*, 136(8), p. 081006.
- [24] Camci, C., and Rizzo, D. H., 2002, "Secondary flow and forced convection heat transfer near endwall boundary layer fences in a 90° turning duct," *Int. J. Heat Mass Transfer*, 45(4), pp. 831-843.
- [25] Aunapu, N. V., Volino, R. J., Flack, K. A., and Stoddard, R. M., 2000, "Secondary Flow Measurements in a Turbine Passage With Endwall Flow Modification," *J. Turbomach.*, 122(4), pp. 651-658.

- [26] Harrison, S., 1990, "Secondary Loss Generation in a Linear Cascade of High-Turning Turbine Blades," *J. Turbomach.*, 112(4), pp. 618-624.
- [27] Vera, M., Blanco, E. d. l. R., Hodson, H., and Vazquez, R., 2009, "Endwall Boundary Layer Development in an Engine Representative Four-Stage Low Pressure Turbine Rig," *J. Turbomach.*, 131(1), p. 011017.
- [28] Holley, B. M., and Langston, L. S., 2009, "Surface Shear Stress and Pressure Measurements in a Turbine Cascade," *J. Turbomach.*, 131(3), pp. 031014-031018.
- [29] Lynch, S. P., 2017, "Three Dimensional Boundary Layer in a Turbine Blade Passage," *AIAA J. Propul. Power*, 33(4), pp. 954-963.
- [30] Cleak, J. G. E., and Gregory-Smith, D. G., 1992, "Turbulence Modeling for Secondary Flow Prediction in a Turbine Cascade," *J. Turbomach.*, 114(3), pp. 590-598.
- [31] Hermanson, K., Kern, S., Picker, G., and Parneix, S., 2003, "Predictions of External Heat Transfer for Turbine Vanes and Blades With Secondary Flowfields," *J. Turbomach.*, 125(1), pp. 107-113.
- [32] Lien, F. S., and Leschziner, M. A., 1999, "Computational Modelling of a Transitional 3D Turbine-cascade Flow using a Modified Low-Re $k - \epsilon$ Model and a Multi-block Scheme," *Int. J. Comput. Fluid Dyn.*, 12(1), pp. 1-15.
- [33] Nagabhushana Rao, V., Tucker, P. G., Jefferson-Loveday, R. J., and Coull, J. D., 2013, "Large eddy simulations in low-pressure turbines: Effect of wakes at elevated free-stream turbulence," *Int. J. Heat Fluid Flow*, 43, pp. 85-95.
- [34] Gross, A., and Sondergaard, R., 2015, "Investigation of Low-Pressure Turbine Endwall Flows: Simulations and Experiments," *Proc. 53rd AIAA Aerospace Sciences Meeting*, Paper AIAA-2015-1290.
- [35] Gross, A., Romero, S., Marks, C., and Sondergaard, R., 2016, "Numerical Investigation of Low-Pressure Turbine Endwall Flows," *Proc. 54th AIAA Aerospace Sciences Meeting*, Paper AIAA2016-0331.
- [36] Gross, A., Marks, C. R., Sondergaard, R., Bear, P. S., and Mitch Wolff, J., 2017, "Experimental and Numerical Characterization of Flow Through Highly Loaded Low-Pressure Turbine Cascade," *J. Propul. Power*, pp. 1-13.
- [37] Gross, A., Marks, C. R., and Sondergaard, R., 2017, "Numerical Investigation of Low-Pressure Turbine Junction Flow," *AIAA J.*, pp. 1-5.
- [38] Cui, J., Nagabhushana Rao, V., and Tucker, P. G., 2017, "Numerical investigation of secondary flows in a high-lift low pressure turbine," *Int. J. Heat Fluid Flow*, 63, pp. 149-157.
- [39] Tyacke, J., Tucker, P., Jefferson-Loveday, R., Rao Vadlamani, N., Watson, R., Naqavi, I., and Yang, X., 2013, "Large Eddy Simulation for Turbines: Methodologies, Cost and Future Outlooks," *J. Turbomach.*, 136(6), pp. 061009-061009.
- [40] Tucker, P. G., 2013, "Trends in turbomachinery turbulence treatments," *Prog. Aerosp. Sci.*, 63, pp. 1-32.
- [41] Lynch, S. P., and Thole, K. A., 2016, "Comparison of the Three-Dimensional Boundary Layer on Flat Versus Contoured Turbine Endwalls," *J. Turbomach.*, 138(4), pp. 041008-041008.
- [42] "ANSYS Fluent: Theory Guide," ANSYS, Inc., Canonsburg, PA.
- [43] Shur, M. L., Spalart, P. R., Strelets, M. K., and Travin, A. K., 2008, "A hybrid RANS-LES approach with delayed-DES and wall-modelled LES capabilities," *Int. J. Heat Fluid Flow*, 29(6), pp. 1638-1649.
- [44] Smirnov, A., Shi, S., and Celik, I., 2001, "Random flow generation technique for large eddy simulations and particle-dynamics modeling," *J. Fluids Engr.*, 123(2), pp. 359-371.
- [45] Lynch, S. P., 2011, "The Effect of Endwall Contouring on Boundary Layer Development in a Turbine Blade Passage," PhD, Virginia Tech, Virginia Tech.
- [46] Hunt, J. C., Wray, A. A., and Moin, P., 1988, "Eddies, Stream, and Convergence Zones in Turbulent Flows," No. CTR-S88.
- [47] David, L., Fraticelli, R., Wieneke, B., and Thomas, L., 2007, "Investigation of three-dimensional vortex structures in crossflow by time-resolved tomographic PIV," *Proc. 7th International Symposium on Particle Image Velocimetry*, pp. 11-14.
- [48] Holstad, A., Andersson, H. I., and Pettersen, B., 2012, "Turbulence in a skewed three-dimensional wall-bounded shear flow: effect of mean vorticity on structure modification," *Int. J. Numer. Methods Fluids*, 69(8), pp. 1299-1325.